

JAAS

Journal of Analytical Atomic Spectrometry

Accepted Manuscript

This article can be cited before page numbers have been issued, to do this please use: M. Kutzschbach, T. Erhardt, M. Mertineit, L. Marko, M. Schramm, L. Richter, W. Nikonow and W. Müller, *J. Anal. At. Spectrom.*, 2026, DOI: 10.1039/D6JA00085A.



This is an Accepted Manuscript, which has been through the Royal Society of Chemistry peer review process and has been accepted for publication.

Accepted Manuscripts are published online shortly after acceptance, before technical editing, formatting and proof reading. Using this free service, authors can make their results available to the community, in citable form, before we publish the edited article. We will replace this Accepted Manuscript with the edited and formatted Advance Article as soon as it is available.

You can find more information about Accepted Manuscripts in the [Information for Authors](#).

Please note that technical editing may introduce minor changes to the text and/or graphics, which may alter content. The journal's standard [Terms & Conditions](#) and the [Ethical guidelines](#) still apply. In no event shall the Royal Society of Chemistry be held responsible for any errors or omissions in this Accepted Manuscript or any consequences arising from the use of any information it contains.

In situ Rb/Sr dating of potassium salt minerals (sylvite and carnallite) by 157 nm LA-ICP-MS/MS

Martin Kutzschbach^{1,2*}, Tobias Erhardt^{1,2}, Michael Mertineit³, Linda Marko^{1,2},
Michael Schramm³, Lisa Richter³, Wilhelm Nikonow³, Wolfgang Müller^{1,2}

¹ Institute of Geosciences, Goethe University Frankfurt, Frankfurt am Main, Germany

² Frankfurt Isotope and Element Research Center (FIERCE), Goethe University Frankfurt, Frankfurt am Main, Germany

³ Bundesanstalt für Geowissenschaften & Rohstoffe (BGR), Hannover, Germany

In preparation for JAAS Communications

*Corresponding author: kutzschbach@em.uni-frankfurt.de

Keywords: in situ Rb-Sr geochronology, carnallite, sylvite, Morsleben, salt minerals, underground storage, hydrogen, natural gas, LA-ICP-MS/MS, 157 nm laser ablation

Abstract

Evaporite deposits are of increasing societal importance as potential repositories for high-level radioactive waste and host lithologies for the subsurface storage of natural gas and hydrogen. In order to conduct robust long-term risk assessments, particularly with respect to the timing of deposition and deformation, the geological history of such deposits must therefore be reconstructed accurately. However, direct geochronometric methods applicable to evaporites remain very limited and ages may only be obtained indirectly via dating of detrital minerals.

Here we report the first application of reaction-cell laser ablation inductively coupled plasma mass spectrometry (LA-ICP-MS/MS) using a recently developed dual-wavelength laser system (193 and 157 nm) to potassium salt minerals (sylvite and carnallite) from the Morsleben site (NE Germany), which is hosted within a salt structure of Permian age. We find that, compared with 193 nm, ablation at 157 nm is more controlled and shows fewer Rb-Sr elemental fractionation. Despite low (6-40 ng/g) strontium concentrations, the salt minerals contain almost exclusively radiogenic ^{87}Sr (~99 %), which enables the determination of precise (~ 3%) single-spot Rb-Sr ages that are effectively independent of the initial $^{87}\text{Sr}/^{86}\text{Sr}$. Kernel density estimates of these single-spot ages reveal four dominant age modes at ~4 Ma, ~14 Ma, ~33 Ma, and ~91 Ma. These ages are consistent with the few previously published data from Morsleben and nearby salt mines and can be linked to regional tectonic events. For the first time, this study demonstrates the potential of in situ LA-ICP-MS/MS as a direct (and fast) geochronological tool for evaporite deposits at a spatial resolution of $\leq 100 \mu\text{m}$.

1
2
3
4
5
6
7
8
9
10
11
12
13
14
15
16
17
18
19
20
21
22
23
24
25
26
27
28
29
30
31
32
33
34
35
36
37
38
39
40
41
42
43
44
45
46
47
48
49
50
51
52
53
54
55
56
57
58
59
60

Open Access Article. Published on 24 April 2016. Downloaded on 4/24/2016 11:47:53 PM.
This article is licensed under a Creative Commons Attribution 3.0 Unported Licence.



1. Introduction

Evaporite deposits are of considerable societal and economic importance. Besides the mineral resources as such, thick salt sequences are widely regarded as suitable host rocks for high-level radioactive waste disposal^{1,2} and for underground storage of natural gas and hydrogen^{3,4,5} due to their low permeability, high thermal conductivity and self-healing behavior.^{6,7,8} In addition, potassium-bearing evaporites constitute a critical raw material for fertilizer production.⁹ These applications require a detailed understanding of the depositional, diagenetic and deformation history of salt deposits, including robust constraints on the timing of salt deposition and subsequent deformation or fluid-rock interaction.

Radiogenic isotope systems provide powerful tools to constrain the timing of geological processes.¹⁰ They allow the determination of crystallization ages of mineral phases, which can also be reset or partially re-equilibrated during recrystallization and dissolution-reprecipitation processes. Such processes commonly accompany major tectonic events or (hydro)thermal fluid circulation and therefore provide a record of deformation, sealing and fluid-flow histories that may overprint evaporite deposits. Isotopic ages thus complement structural geological analyses and regional geological reconstructions.

Apart from pioneering studies, relatively few attempts have been made to directly date salt minerals using isotopic methods. These include K-Ar and ⁴⁰Ar/³⁹Ar dating of potassium- and magnesium-bearing sulfates such as polyhalite, leonite, langbeinite, kieserite, and kainite.¹¹⁻²¹ K-Ca dating has been applied to sylvite and carnallite,²²⁻²⁵ while Sm-Nd dating has been used for intrasalary magnesite.²⁶ Rb-Sr dating has also been applied to sylvite, carnallite, and langbeinite.^{14,25,27-31}

Importantly, all these examples were limited in spatial resolution. While applications of the Sm-Nd, K-Ca, and Rb-Sr geochronometers to salts have thus far required dissolution of substantial amounts of sample material (e.g. gram-kilogram-scale samples for the ID-TIMS analyses of

1
2
3
4
5
6
7
8
9
10
11
12
13
14
15
16
17
18
19
20
21
22
23
24
25
26
27
28
29
30
31
32
33
34
35
36
37
38
39
40
41
42
43
44
45
46
47
48
49
50
51
52
53
54
55
56
57
58
59
60

Open Access Article. Published on 24 April 2026. Downloaded on 4/24/2026 11:47:55 PM.
This article is licensed under a Creative Commons Attribution 3.0 Unported Licence.



1
2
3 carnallite)^{28,30}, K-Ar and ⁴⁰Ar/³⁹Ar case studies have involved laser heating of comparatively large
4 quantities of material (e.g., aliquots of ~50 mg were used for the K-Ar analyses of Wójtowicz et
5 al., 2003 and several grains of 200-250 μm size were required for the ⁴⁰Ar/³⁹Ar analyses of Leitner
6 et al., 2022)^{18,21}. Such bulk or semi-bulk approaches risk co-analyzing fluid inclusions or mineral
7 impurities, potentially biasing age results. Moreover, small-scale domains affected by
8 recrystallization or dissolution-reprecipitation during fluid interaction are likely to remain
9 undetected.

10
11
12 Modern laser-based in situ dating techniques offer substantially higher spatial resolution, typically
13 consuming only a few 100s of ng of sample material and hence offering the ability to directly target
14 specific microstructural domains. However, despite their widespread application to silicates (mica,
15 feldspar, amphiboles, zircon), oxides (rutile, magnetite), and phosphates (apatite, monazite), such
16 methods have not yet been successfully applied to salt minerals. The only notable exception is in
17 situ U-Pb dating of sulfates such as gypsum and anhydrite,^{32,33} which are common constituents of
18 evaporite sequences. Other in situ geochronological applications in salt-bearing successions have
19 focused on accessory minerals embedded within the salt formation, such as volcanic apatite or
20 detrital zircon and rutile, to indirectly constrain depositional ages.^{34,35}

21
22
23 Potassium-bearing salt minerals, particularly sylvite (KCl) and carnallite (KMgCl₃·6H₂O),
24 represent promising targets for in situ Rb-Sr geochronology using laser ablation inductively
25 coupled plasma tandem mass spectrometry (LA-ICP-MS/MS). These minerals are widespread
26 primary (for sylvite under the condition of MgSO₄ depleted seawater) and secondary constituents
27 of evaporite deposits and, due to the similar ionic radii of Rb⁺ and K⁺,³⁶ are expected to contain
28 elevated Rb concentrations, yet little common-Sr, resulting in elevated Rb/Sr-ratios and thus
29 sufficient ingrowth of radiogenic ⁸⁷Sr. Furthermore, compared to the K-Ar system, the Rb-Sr
30 system is expected to be more retentive during secondary (hydro)thermal events.^{37,38} This is
31
32
33
34
35
36
37
38
39
40
41
42
43
44
45
46
47
48
49
50
51
52
53
54
55
56
57
58
59
60

supported by the lower closure temperatures reported for K-Ar in muscovite (approximately 350-450 °C) relative to Rb-Sr in muscovite (~500–650°C).³⁹⁻⁴⁴ To date, no systematic study has examined the relative closure temperatures of the K-Ar and Rb-Sr systems in K-salt minerals. Nevertheless, early investigations into the retentivity of Ar in sylvite indicate that Ar diffusion increases drastically at temperatures exceeding 40 °C.^{45,46} Moreover ⁴⁰Ar/³⁹Ar geochronology requires neutron irradiation, which involves access to nuclear facilities, handling of activated materials and hence imposes significant logistical constraints. As a result, the time from sample preparation to analysis can extend over several months. Even after irradiation, individual analyses typically require approximately 1-2 hours, which is considerably longer than in situ Rb-Sr measurements by LA-ICP-MS/MS. As already mentioned solution-based ID-TIMS Rb-Sr dating has already been successfully applied to salt minerals and there have been successful attempts to overcome limitations in spatial resolution through microdrilling and laser cutting sampling techniques, which have reduced ID-TIMS sample sizes to a few tens of µg.^{47,48} However, these µ-ID-TIMS studies targeted Sr-rich minerals such as mica, which contain several tens of µg/g Sr and exhibit comparatively moderate ⁸⁷Rb/⁸⁶Sr ratios (often <100). This is contrasted by K-salt minerals, which are typically characterized by extreme ⁸⁷Rb/⁸⁶Sr ratios (up to several million) and low Sr concentrations (down to < 10 ng/g).²⁹ This poses two analytical challenges. First, the extremely high Rb/Sr ratios complicate the separation of Rb and Sr in conventional wet-chemical approaches and residual ⁸⁷Rb may cause isobaric interference on ⁸⁷Sr.^{49,50} In contrast, the separation of Rb and Sr using a collision reaction cell (CRC) in LA-ICP-MS/MS analyses is considered quantitative. Within the CRC, reactive gases (O₂, SF₆, N₂O, CH₃F) form Sr-molecule ions such as SrF⁺ or SrO⁺ that can be measured free of the ⁸⁷Rb-interference.⁵¹⁻⁵⁵ The efficiency of the CRC-based purification process has already been demonstrated by Zack & Hogmalm.⁵¹ When using O₂ as a reactive gas, they observed no detectable signal at mass 101 (⁸⁵Rb¹⁶O) during

1
2
3
4
5
6
7
8
9
10
11
12
13
14
15
16
17
18
19
20
21
22
23
24
25
26
27
28
29
30
31
32
33
34
35
36
37
38
39
40
41
42
43
44
45
46
47
48
49
50
51
52
53
54
55
56
57
58
59
60

Open Access Article. Published on 24 April 2026. Downloaded on 4/24/2026 11:47:53 PM.
This article is licensed under a Creative Commons Attribution 3.0 Unported Licence.



1
2
3 ablation of pure RbCl, despite a signal of 10^9 cps on mass 85 (^{85}Rb). Second, the very low Sr
4 concentrations in K salts necessitate stringent blank control and ultimately increase the minimum
5 amount of sample required for a single analysis. In previous studies the total mass of Sr analyzed
6 was typically <10 ng, while blank levels were maintaining below 10 pg, corresponding to
7 approximately 1‰ blank contributions.^{47,48} Given that Sr concentrations in K salts are
8 roughly three orders of magnitude lower than in mica (ng/g vs. $\mu\text{g/g}$), achieving 1‰ blank levels
9 would require a proportional increase in sample size on the order of tens of milligrams.
10
11 Consequently, the spatial resolution offered by LA-ICP-MS/MS is effectively unattainable using
12 ID-TIMS techniques. Third, ID-TIMS analyses typically require several days per sample,
13 including dissolution, spike equilibration, and chromatographic purification, with measurement
14 times lasting several hours. Consequently, analytical throughput is limited to only a few samples
15 per month per instrument. In contrast, LA-ICP-MS/MS enables in situ measurements within
16 minutes, representing an improvement in throughput of several orders of magnitude.
17
18 In this study, we present the first successful in situ laser-based in situ Rb-Sr dating of the K-salt
19 minerals sylvite and carnallite and thus demonstrate the feasibility of high-spatial-resolution
20 geochronology directly applied to evaporite minerals. This advance was enabled by exploiting the
21 superior ablation behavior of K salts at 157 nm compared to 193 nm, where these matrices ablate
22 poorly, similar to other challenging materials such as gypsum and barite. In these materials, 193
23 nm laser radiation penetrates substantially deeper than 157 nm radiation,⁵⁶ which can lead to
24 uncontrolled ablation. Moreover, previous studies indicate that 157 nm ablation produces reduced
25 elemental and isotopic fractionation relative to longer wavelengths,^{57,58} which is advantageous for
26 Rb-Sr geochronology given the strong matrix-dependent fractionation of Rb and Sr combined with
27 the lack of suitable matrix matched secondary reference materials.
28
29
30
31
32
33
34
35
36
37
38
39
40
41
42
43
44
45
46
47
48
49
50
51
52
53
54
55
56
57
58
59
60

2. Materials and Methods

2.1 Material

All samples originate from the Morsleben site (NE, Germany), located within the Allertal zone, a NW–SE trending fault system. Upper Permian (Zechstein) salt migrated into these faults in several phases from the Mesozoic to the Cenozoic and subsequently experienced intense deformation.^{59–61} The site was used for the disposal of low- to intermediate-level radioactive waste between 1971 and 1998. Preparations for the repository's closure are currently underway. The samples were collected at and near the “Bunte First”, an extensive vein mineralization (m to 10 m scale) hosted within fractured anhydrite rocks.⁶² This style of mineralization indicates a secondary, and therefore younger, origin of the minerals compared to the Zechstein depositional age. The assemblage comprises carnallite, sylvite, polyhalite, and commonly purple to dark blue halite. From this locality, we selected a macroscopically homogeneous carnallite sample (CT3) from the drill core archive of the “Bundesanstalt für Geowissenschaften und Rohstoffe” (BGR) in Hannover. A detailed description of this sample is provided in Mertineit et al. (2015)³¹. The samples were transported in sealed plastic bags to the University of Frankfurt and were placed into a desiccator on the same day to minimize alteration due to exposure to atmospheric humidity. A few weeks later all samples were cut to size using a rotating steel saw without water cooling. The resulting pieces were then embedded in a 1-inch epoxy resin block, impregnated several times with epoxy and dry-polished using silicon carbide (SiC) abrasive papers (grit 400 up to 2000). The final epoxy mounts were sealed in plastic bags and placed in a desiccator. For transport from Goethe Universität Frankfurt to the BGR, the bags were additionally filled with hygroscopic silica gel. Reflected light images of the mounts are provided in Fig. 1. Further description of the samples is given in the supplementary material.

2.2 Reflected light and electron microscopy.

We tested the ablation behavior of the K-salt samples using 193nm and 157nm laser wavelength. High-resolution secondary electron (SE) images of the ablation pits (Fig. 2) were acquired using a FEI Quanta 650F field emission scanning electron microscope at the BGR Hanover (pressure = 0.6 mbar, accelerating voltage = 15 kV, working distance = 13.6 mm). Additionally, the depth of the ablation pits was determined under reflected light using an optical digital microscope (Keyence VHX) at the Goethe University Frankfurt.

2.3 μ X-Ray Fluorescence

The mineralogy and homogeneity on a micro-scale were verified by micro-energy-dispersive X-ray fluorescence microscopy (μ -XRF) using a M4 Tornado Plus from Bruker Nano. The device operates with a Rh tube at 50 kV and 600 μ A with a spot size of about 20 μ m at 17.4 keV focused by a poly-capillary lens.⁶³ The sample chamber is evacuable to 2 mbar, thereby enhancing detection limits and permitting measurement of elements as light as carbon. The mounts were measured with a step size of 20 μ m and a dwell time of 20 ms per pixel. The measured data were analyzed with the M4 Tornado software and the results are presented as element distribution maps with element intensities in false colors. Element quantification is done using the standardless Fundamental Parameter method.

2.4. In situ Rb-Sr dating and trace element analyses by LA-ICP-MS/MS

Single spot *in situ* Rb-Sr dating and trace element analyses of sylvite and carnallite was performed at the FIERCE Laboratory of Goethe University Frankfurt using a reaction cell laser ablation inductively coupled plasma mass spectrometry system (LA-ICP-MS/MS) and overall follows Kutzschbach et al. 2026.⁶⁴ The latter comprises an Agilent 8900 spectrometer coupled to a custom-

1
2
3
4
5
6
7
8
9
10
11
12
13
14
15
16
17
18
19
20
21
22
23
24
25
26
27
28
29
30
31
32
33
34
35
36
37
38
39
40
41
42
43
44
45
46
47
48
49
50
51
52
53
54
55
56
57
58
59
60

Open Access Article. Published on 24 April 2026. Downloaded on 4/24/2026 11:47:55 PM.
This article is licensed under a Creative Commons Attribution 3.0 Unported Licence.



built Dual-Wavelength (157 & 193 nm) LA system.⁵⁶ Specifically, the analytical setup comprised a RESolution-SE laser ablation system (Applied Spectra Inc., USA) equipped with an S-155 laser ablation cell (Laurin Technic, Australia) and two excimer lasers that in part have separate beam delivery systems: an ExciStar 500 (193 nm) and a Coherent COMPex F2 (157 nm). Both lasers deliver beams with a higher order super gaussian intensity distribution but varying pulse length of 7ns (193 nm) and 20ns (157 nm). The latter was used for all analytical measurements. Spot sizes of 104 μm , a fluence of 2.5 J/cm² and a laser repetition rate of 10 Hz was applied. For LA-ICP-MS/MS coupling, a “squid” signal-smoothing device (Laurin Technic)⁶⁵ was employed to improve signal stability. Ablation took place in He (0.3 l/min) to which Ar (0.95 l/min) + N₂ (3.5 ml/min) was added from the top of the ablation funnel, whose stepwise geometry prevents He-Ar-N₂ mixing directly at the ablation site. Pure (99.999%) nitrous oxide (N₂O) at a flow rate of 0.193 ml/min gas was used as a reactive cell gas to resolve the isobaric interference of ⁸⁷Rb and ⁸⁷Sr through measuring ⁸⁶Sr, ⁸⁷Sr, ⁸⁸Sr as mass-shifted ^{86/87/88}Sr¹⁶O⁺ (70 ms/sweep each). Rb was acquired as ⁸⁵Rb ‘on-mass’ (50 ms/sweep) to avoid interference of residual on-mass ⁸⁷Sr with ⁸⁷Rb. The formation of RbO⁺ is negligible (zero counts per second (cps) were recorded at m/z = 101). Moreover, the following nuclides were recorded (dwell times in ms brackets): ⁷Li (5), ¹¹B (5), ²³Na¹⁶O (5), ²⁴Mg (2), ²⁷Al (2), ²⁸Si³²O₂ (5), ³⁴S¹⁶O (2), ³⁵Cl¹⁶O (10), ⁴¹K (2), ⁴³Ca (2), ⁷⁹Br (10), ⁸¹Br (10), ¹²⁷I (10), ¹³³Cs (5), ¹³⁷Ba (5), ²⁰⁸Pb (2), ²³⁸U (2) . The sweep time was 382 ms. The following reference materials were used: NIST 610, NIST612, BHVO-2G, GSD-1F, GSE-1G, CGL026 halite that was pressed into an ablatable pellet using a hydraulic press, SagaB biotite, SagaB alkali feldspar, 98973 muscovite and Phalaborwa biotite.⁶⁶⁻⁷¹ More detailed information regarding the ICP-MS/MS and laser settings are compiled in Table S1.

Rb-Sr isotopic and chemical data were reduced using the LADR Software.⁷² Isotope ratios are calculated as inverse ratios (⁸⁷Rb/⁸⁷Sr and ⁸⁶Sr/⁸⁷Sr) based on a ratio-of-means approach and

1
2
3
4
5
6
7
8
9
10
11
12
13
14
15
16
17
18
19
20
21
22
23
24
25
26
27
28
29
30
31
32
33
34
35
36
37
38
39
40
41
42
43
44
45
46
47
48
49
50
51
52
53
54
55
56
57
58
59
60

Open Access Article. Published on 24 April 2026. Downloaded on 4/24/2026 11:47:53 PM.
This article is licensed under a Creative Commons Attribution 3.0 Unported Licence.



discarding the first 3s of the signal (rise time and surface contamination). Whenever conventional isotope ratios are reported, they are derived from the processed inverse ratios rather than being calculated independently from the raw data.

Gas-blank and drift-corrected $^{87}\text{Rb}/^{87}\text{Sr}$ were corrected for mass bias using NIST610 ($^{87}\text{Rb}/^{87}\text{Sr} = 3.3638 \pm 0.0071$; $^{86}\text{Sr}/^{87}\text{Sr} = 1.409048 \pm 0.000036$) and $^{86}\text{Sr}/^{87}\text{Sr}$ ratios using NIST612 ($^{87}\text{Rb}/^{87}\text{Sr} = 1.633 \pm 0.021$; $^{86}\text{Sr}/^{87}\text{Sr} = 1.410312 \pm 0.000040$); $^{86}\text{Sr}/^{87}\text{Sr}$ from Woodhead and Hergt (2001)⁶⁶; $^{87}\text{Rb}/^{87}\text{Sr}$ from certified Rb/Sr concentrations.^{67,68} The P/A factor is tuned once at the beginning of the session in MS/MS mode⁶⁴ and the P/A crossover value is set to 10^7 cps times the P/A factor, with the latter being ~ 0.183 for $^{86+16}\text{Sr}$, ~ 0.177 for $^{87+16}\text{Sr}$, ~ 0.185 for $^{88+16}\text{Sr}$ and ~ 0.188 for ^{85}Rb . However, as we observe significant drift of the P/A factor (up to 0.4% per hour but varying from session to session), we applied P/A matched calibration of $^{86}\text{Sr}/^{87}\text{Sr}$ and $^{87}\text{Rb}/^{87}\text{Sr}$ ratios. NIST SRM 612 was used as the primary reference material for the calibration of $^{86}\text{Sr}/^{87}\text{Sr}$ ratios using $^{86+16}\text{Sr}$ and $^{87+16}\text{Sr}$, which were both recorded in pulse mode similar to all samples and secondary reference materials except for CGL analysis #001 (here both $^{86+16}\text{Sr}$ and $^{87+16}\text{Sr}$ in analog mode) and BHVO-2G analysis #001-003 (here $^{86+16}\text{Sr}$ in analog). NIST SRM 610 had both $^{86+16}\text{Sr}$ and $^{88+16}\text{Sr}$ in analog mode and $^{87+16}\text{Sr}$ in pulse mode and hence was not an alternative for calibration. Due to the P/A bias, these analyses were not further considered. In contrast, the $^{87}\text{Rb}/^{87}\text{Sr}$ ratios were calibrated using NIST SRM 610, because ^{85}Rb was consistently measured in analog mode, whereas $^{87+16}\text{Sr}$ was measured in pulse mode. An exception applies to SagaB alkali feldspar analyses #012 and #019-021, in which ^{85}Rb was measured in pulse mode; for these analyses, $^{87}\text{Rb}/^{87}\text{Sr}$ ratios were calibrated using NIST SRM 612. This approach ensures appropriate pulse/analog (P/A) matching between samples and reference materials in all cases. Downhole fractionation of $^{87}\text{Rb}/^{87}\text{Sr}$ ratios over the ablation interval was modelled with a cubic polynomial.

1
2
3
4
5
6
7
8
9
10
11
12
13
14
15
16
17
18
19
20
21
22
23
24
25
26
27
28
29
30
31
32
33
34
35
36
37
38
39
40
41
42
43
44
45
46
47
48
49
50
51
52
53
54
55
56
57
58
59
60

Open Access Article. Published on 24 April 2026. Downloaded on 4/24/2026 11:47:55 PM.
This article is licensed under a Creative Commons Attribution 3.0 Unported Licence.



Matrix corrected $^{87}\text{Rb}/^{87}\text{Sr}$ ratios were obtained using the expected age (2058.2 +/- 7 Ma)⁷¹ and the measured isochron age of the Phalaborwa RM (1966.4 +/- 9.1 Ma) and the following equation:

$$(1) \quad (^{87}\text{Rb}/^{87}\text{Sr})_{\text{matrix corrected}} = (^{87}\text{Rb}/^{87}\text{Sr}) \cdot \frac{e^{[(RM_{\text{age,measured}}*\lambda)-1]}}{e^{[(RM_{\text{age,expected}}*\lambda)-1]}}$$

with λ being the ^{87}Rb decay constant.⁷³ External uncertainties, i.e. the uncertainty of λ , NIST isotope ratios and the Phalaborwa expected age and its reproducibility, were added to the internal uncertainty in quadrature to obtain the fully propagated uncertainty. No statistically significant excess scatter neither within-run nor long-term has been detected for the NIST610 isotope ratios. For the isochron ages of the reference materials, the internal uncertainty is constrained by the uncertainty resulting from the isochron fit. Model single spot ages were calculated for the K-salts by applying an initial $^{87}\text{Sr}/^{86}\text{Sr}$ isotope ratio of 0.75 +/- 0.05. Here, the uncertainty introduced by the uncertainty of the initial $^{87}\text{Sr}/^{86}\text{Sr}$ isotope ratio is included in the fully propagated uncertainty of single spot ages. Isochron ages and single spot ages were calculated using IsoplotR.⁷⁴

The chemical composition was determined through calibration with NIST610 for Li, B, Na, Mg, Al, Si, S, K, Ca, Cs, Ba, Pb and U as the primary reference material. The halogens Cl, Br, and I were calibrated based on GSE-1G applying the values determined by the noble gas method published in Marks et al. (2017).⁷⁵ All mica RM, SagaB alkalifeldspar, BHVO, GSD-1G and NIST612 were normalized using Si as an internal standard.^{69,71} CGL026 was normalized using Na as an internal standard. All sylvite and carnallite analyses were normalized to K assuming stoichiometric K concentrations. CGL026 was normalized using Na as an internal standard. All sylvite and carnallite analyses were normalized to K assuming stoichiometric K concentrations of 52.45 wt% and 14.07 wt%, respectively.

3. Results & Discussion

3.1 Ablation behavior at 157nm

We evaluated the ablation characteristics of carnallite and sylvite by imaging the resulting crater pits at 193 nm (spot diameter of 80 μm and 1.5 J/cm^2) and 157 nm (spot diameter of 104 μm and 2.5 J/cm^2) wavelengths using secondary electron microscopy (Fig. 2). Craters generated at 157 nm display smooth and well-defined edges, whereas ablation at 193 nm results in pronounced chipping and irregular crater margins, indicating less controlled ablation behavior. Owing to the more stable ablation and significantly lower ablation rates, all subsequent analyses were therefore performed using the 157 nm wavelength. The resulting signals are smooth (Fig. 3) with low RSD% values, e.g. $\sim 1\%$ for $^{24}\text{Mg}/^{41}\text{K}$ and $^{85}\text{Rb}/^{41}\text{K}$ and $\sim 3.5\%$ for $^{87}\text{Sr}/^{41}\text{K}$ in carnallite. Normalization to the internal standard (^{41}K) is applied to account for the overall downhole decrease in sensitivity, commonly observed during static spot ablation.

In addition to the SEM imaging, the crater depth and associated average per pulse ablation rate of carnallite, sylvite, NIST610 and the mica RM was determined using an optical digital microscope (Keyence VHX). For sylvite even at relatively low fluences of 1.5 J/cm^2 , the average ablation rate at 193 nm is ~ 700 nm per pulse, whereas at 157 nm a $\sim 30\%$ lower ablation rate of ~ 500 nm per pulse is obtained, despite the higher fluence at 157 nm of 2.5 J/cm^2 . For carnallite, the difference in ablation rate between the two wavelength is even more pronounced. At 157 nm and a fluence of 2.5 J/cm^2 , an ablation rate of approximately 400 nm per pulse was obtained. In contrast, at 193 nm and a fluence of 1.5 J/cm^2 , the resulting craters were too deep to bring their bottom into focus. Based on our experience, this indicates crater depths exceeding ~ 300 μm , corresponding to ablation rates of ≥ 1 μm per pulse. The large depth of the CT3 craters is also illustrated in Fig. 2e. The high

1
2
3 ablation rates at 193 nm are attributed to the lower threshold fluence and greater absorption depth
4 for K-salts at 193 nm⁵⁶ and would lead to rapidly increasing ablation depth during analysis in turn
5 leading to undesirably high down-hole fractionation and overall reduction of aerosol transport. For
6 the other materials, the difference in ablation rate is insignificant within the measurement
7 uncertainty (~10 %, 2SD). For NIST610 and the mica RM average ablation rates of ~100 and ~80
8 nm have been determined at 157 (2.5 J/cm²) and 193 nm (1.5 J/cm²), respectively.
9

3.2 Rb-Sr downhole fractionation

10
11
12 In contrast to the downhole fractionation (DHF) behavior of the mica reference material (RM),
13 which closely follows that of NIST 610 and is characterized by a monotonically increasing
14 ⁸⁷Rb/⁸⁷Sr ratio over the ablation interval, the wavy DHF patterns observed in carnallite and sylvite
15 differ markedly. These K-bearing salts exhibit a 1-3% increase in ⁸⁷Rb/⁸⁷Sr during the first third of
16 the ablation, followed by a 1-2 % decrease in the second third and a renewed increase of ~1% in
17 the final third. Importantly, the overall magnitude of DHF in carnallite and sylvite is lower than
18 that observed for NIST 610 and the mica RM, with maximum fractionation of approximately 1%
19 for carnallite and 3% for sylvite, compared to values of up to ~5% for the reference materials. This
20 is remarkable considering the ~5 times higher ablation rates obtained for the K-salts compared to
21 for example the mica RM (see section 3.1) as higher aspect ratios (depth/width) generally promote
22 stronger downhole fractionation. Consequently, no DHF correction was applied to the K-salt
23 analyses, as application of a NIST 610-based DHF correction would result in overcorrection of the
24 measured ⁸⁷Rb/⁸⁷Sr ratios. In contrast, NIST 610 was used for downhole correction of all reference
25 materials, resulting in improved precision of the ⁸⁷Rb/⁸⁷Sr ratios (for example, the mean precision
26 of the 98973 muscovite RM improves from 0.72% to 0.62%). A constant ablation interval was
27 maintained for all reference materials and for the vast majority of K-salt analyses. Ablation
28
29
30
31
32
33
34
35
36
37
38
39
40
41
42
43
44
45
46
47
48
49
50
51
52
53
54
55
56
57
58
59
60

intervals were only subdivided when compositional variations within a single interval significantly exceeded analytical uncertainty and residual downhole bias, indicating multiple age domains (e.g., carnallite analysis #005: 14.6 ± 0.41 Ma and 5.8 ± 0.22 Ma; see Table S1). In other instances, ablation intervals had to be shortened to avoid mixed analyses, such as the complex sylvite-halite-kieserite mixtures in sample P10.

It is important to note that omitting DHF corrections does not affect accuracy when the same ablation interval is used for both samples and RM; however, it does lead to reduced precision. If, however, the ablation interval differs from that of the primary RM, a systematic bias is introduced; based on the DHF curves (Fig. 3), this bias is not expected to exceed 3% in case of the K-salts.

3.3 Rb/Sr isotope ratios, ages and elemental chemistry of K-salt minerals

The sample specific limits of detection (LOD) were calculated following the approach of Longerich et al. (1996)⁷⁶ and mean LOD values are <0.5 ng/g for Sr and <0.7 ng/g for Rb. In sylvite and carnallite, non-radiogenic ^{86}Sr and ^{88}Sr were frequently below the (nominal) detection limit. In these cases, the corresponding values were replaced by $\text{LOD}/\sqrt{2}$ following the approach of Frenzel (2023).⁷⁷ In contrast, ^{87}Sr is much more abundant and reaches mean concentrations of 5-6 ng/g in CT3 and 17-39 ng/g in sylvites P3 and P10, respectively. Given the high Rb concentrations of 330-340 $\mu\text{g/g}$ in CT3 carnallite and 46-110 $\mu\text{g/g}$ in P3 and P10 sylvites, virtually all the measured ^{87}Sr (98.5–99.6%) is attributable to radiogenic ingrowth. Single-spot Rb-Sr analyses of carnallite CT3 yield extremely high $^{87}\text{Rb}/^{86}\text{Sr}$ ratios on the order of $\sim 4 \cdot 10^5$ to $\sim 1.2 \cdot 10^7$, reflecting the strongly Rb-enriched and common Sr-poor carnallite chemistry. Corresponding $^{87}\text{Sr}/^{86}\text{Sr}$ ratios are highly radiogenic, ranging from ~ 5 to 2260. Sylvite samples P3 and P10 display elevated but slightly less extreme $^{87}\text{Rb}/^{86}\text{Sr}$ ratios compared to carnallite. In sylvite P3, $^{87}\text{Rb}/^{86}\text{Sr}$ ratios range from $\sim 1.2 \cdot 10^5$

1
2
3
4
5
6
7
8
9
10
11
12
13
14
15
16
17
18
19
20
21
22
23
24
25
26
27
28
29
30
31
32
33
34
35
36
37
38
39
40
41
42
43
44
45
46
47
48
49
50
51
52
53
54
55
56
57
58
59
60

Open Access Article. Published on 24 April 2025. Downloaded on 4/24/2026 11:47:55 PM.
This article is licensed under a Creative Commons Attribution 3.0 Unported Licence.



1
2
3 to $\sim 2.3 \times 10^6$, whereas sylvite P10 exhibits lower and more restricted ratios between $\sim 3 \times 10^4$ and
4 $\sim 1.5 \times 10^5$. Corresponding $^{87}\text{Sr}/^{86}\text{Sr}$ ratios in P3 range from ~ 50 to ~ 800 and from ~ 40 -160 in P10.
5
6 Individual $^{87}\text{Sr}/^{86}\text{Sr}$ analyses are characterized by relatively poor precision, with 2σ uncertainties
7 ranging from ~ 6 to $\sim 250\%$, which is attributed to the extremely low abundance of non-radiogenic
8 Sr, commonly close to or below the detection limit.
9

10
11 Model single spot ages were calculated applying an initial $^{87}\text{Sr}/^{86}\text{Sr}$ ratio of 0.75 with a
12 conservatively enlarged uncertainty of ± 0.5 . This range was selected to encompass the $^{87}\text{Sr}/^{86}\text{Sr}$
13 ratio of 0.70676-0.70776 reported for Permian seawater,⁷⁸ reflecting Sr incorporation during
14 primary sedimentation, while also allowing for the introduction of additional radiogenic ^{87}Sr
15 during diagenesis, fluid interaction and metamorphic overprint. However, given the radiogenic
16 nature of the investigated K salts, the influence of the assumed initial Sr isotopic composition on
17 the resulting Rb-Sr ages is negligible.⁷⁹ To illustrate this insensitivity, an intentionally extreme
18 (and entirely implausible) initial $^{87}\text{Sr}/^{86}\text{Sr}$ ratio of 2.7 ± 2.0 was tested. Even under this extreme
19 assumption, the single-spot age uncertainty increases by only $\sim 0.13\%$, and the mean age shifts by
20 $\sim 1.1\%$ towards younger values relative to the chosen ratio of 0.75 ± 0.5 . The uncertainty of the
21 latter ratio contributes only an additional $\sim 1.2 \times 10^{-5} \%$ to the total single spot age uncertainty
22 budget, which amounts to a mean relative 2σ uncertainty of $\sim 3\%$ (Fig. 4, Table S1). Previous Rb-
23 Sr ID-TIMS analyses performed on carnallite yield an age precision of 1-2% (2 RSD, see
24 supplementary Table S2) per analysis. This difference in precision is modest, despite the
25 substantially higher precision of Sr isotope ratio measurements obtained by ID-TIMS (tens of
26 ppm; Supplementary Table S2) compared to LA-ICP-MS/MS (tens of percent; Supplementary
27 Table S1). The reason is that, at such extreme Rb/Sr ratios, age precision is dominated by the
28 uncertainty in the Rb/Sr ratio. This uncertainty is of similar magnitude for LA-ICP-MS/MS
29 ($\sim 3\%$) and ID-TIMS (1–2%).
30
31
32
33
34
35
36
37
38
39
40
41
42
43
44
45
46
47
48
49
50
51
52
53
54
55
56
57
58
59
60

1
2
3
4
5
6
7
8
9
10
11
12
13
14
15
16
17
18
19
20
21
22
23
24
25
26
27
28
29
30
31
32
33
34
35
36
37
38
39
40
41
42
43
44
45
46
47
48
49
50
51
52
53
54
55
56
57
58
59
60

Single-spot Rb-Sr ages of carnallite CT3 and sylvite samples P3 and P10 define distinct age distributions. Carnallite CT3 comprises two spatially and geochemically distinct regions of interest (ROI1: analyses #001- #038; ROI2: analyses #039-#050), represented by spot clusters sampled approximately ~1 cm apart (Fig. 1). ROI1 yields older single-spot ages ranging from ~5.8 to ~21.6 Ma, whereas ROI2 defines a younger population between ~0.7 and ~8.8 Ma. Adaptive Kernel density estimates (KDE) of CT3 single-spot ages reveals a clear bimodal distribution with modes at ~4 Ma and ~14 Ma (Fig. 4), consistent with the presence of two age populations. This subdivision into ROIs is supported by distinct trace-element compositions, particularly regarding B and Cs concentrations. ROI1 is characterized by mean B concentrations of 0.29 ± 0.03 ppm (2SE) and mean Cs concentrations of 12.09 ± 0.13 ppm (2SE), whereas ROI2 exhibits ~twofold higher mean B concentrations of 0.64 ± 0.03 ppm (2SE) and slightly lower mean Cs concentrations of 11.57 ± 0.18 ppm (2SE); Table 1. Sylvite P10 displays a unimodal age distribution with a KDE mode centered at ~91 Ma. In contrast, sylvite P3 exhibits more complex age systematics, characterized by a dominant KDE mode at ~33 Ma, subordinate modes at ~26 Ma and ~39 Ma, two analyses yield ages around ~13 Ma, and one analysis records an older age of ~47 Ma. No correlation is detected between trace-element chemistry and Rb-Sr single-spot ages for sylvite P10 or P3.

3.4 Accuracy of the single spot ages of sylvite and carnallite

No matrix-matched secondary reference material is available to directly assess the accuracy of the Rb-Sr ages obtained for K-salt minerals. Nevertheless, the ages obtained for the mica reference materials muscovite 98973 (265.5 ± 2.3 Ma with *c*-axis oriented perpendicular to the incident laser beam, and 268.9 ± 2.1 Ma with *c*-axis parallel to the incident laser beam), as well as for the SagaB alkali feldspar (295.5 ± 6.7 Ma), agree well with their expected ages (98973: 266.8 ± 1.6 Ma; SagaB alkali feldspar: 295.4 ± 1.4 Ma; ID-TIMS analyses of Kutzschbach & Glodny 2024).⁷¹ The

SagaB biotite yields a slightly older age than expected (300.2 ± 2.6 Ma versus 295.4 ± 1.4 Ma)⁷¹ although the resulting bias is limited to ~1%.

It is noteworthy that the Rb-Sr elemental fractionation at 157 nm is substantially smaller than that typically observed at 193 nm. For example, the uncorrected age obtained for the matrix reference material Phalaborwa biotite at 157 nm is 1966.4 ± 9.1 Ma, compared to its expected age of 2058.2 ± 7 Ma,⁷¹ corresponding to a matrix-bias of only ~5%. In contrast, matrix biases at 193 nm are commonly significantly larger, typically on the order of ~10%.^{64, 71, 80-83} Consequently, although a matrix-matched reference material for K salts is currently lacking, any systematic age offset associated with Rb/Sr elemental fractionation at 157 nm is expected to be much smaller than at 193 nm.

Further support of the obtained K-salt ages comes from the available, albeit limited, literature data. Age distributions compatible with the bimodal Rb-Sr age distribution observed for CT3 carnallite (KDE modes at ~14 Ma and ~4 Ma) are reported from the nearby Gorleben salt dome, which shares a similar genetic and tectonic evolution with the one in Morsleben. There, Rb-Sr ID-TIMS analyses of carnallite from the Permian Straßfurth bed yielded model ages between 6 and 14 Ma (assuming an initial $^{87}\text{Sr}/^{86}\text{Sr}$ of 0.707, typical of Permian seawater), interpreted as partial isotopic resetting due to ^{87}Sr loss induced by recrystallization associated with diapiric movement.³⁰ Notably, undeformed primary carnallite from the Pöthen mine (Thuringia, Germany) records a comparable reset age of 14.6 ± 11.1 Ma (isochron age recalculated using the ^{87}Rb decay constant of Villa et al. 2015)⁶⁴, indicating that isotopic resetting was not exclusively controlled by deformation but likely involved temperature- or fluid-assisted processes. Philippe and Haack (1997)³⁰ also documented a younger generation of carnallite occurring as fracture fillings within a 50-80 m thick anhydrite unit that underwent brittle deformation during late Gorleben diapirism, yielding significantly younger ages of 0.6-6.9 Ma.

1
2
3
4
5
6
7
8
9
10
11
12
13
14
15
16
17
18
19
20
21
22
23
24
25
26
27
28
29
30
31
32
33
34
35
36
37
38
39
40
41
42
43
44
45
46
47
48
49
50
51
52
53
54
55
56
57
58
59
60

Open Access Article. Published on 24 April 2026. Downloaded on 4/24/2026 11:47:53 PM.
This article is licensed under a Creative Commons Attribution 3.0 Unported Licence.



The distinct B and Cs concentrations associated with the two different age modes of CT3 suggest that the younger age population may result from fluid-induced isotopic resetting, given that both B and Cs are fluid-mobile elements. Accordingly, the observed geochemical differences between the ROIs are consistent with dissolution-reprecipitation or fluid-assisted recrystallization processes that could partially or fully reset the Rb-Sr system. Episodic fluid flow in the upper Cenozoic may have been associated with the Rhine rift system, which remained active throughout the Cenozoic until the present.⁷⁵ Moreover, a piece of CT3 carnallite was previously analyzed by ID-TIMS, yielding an age of 16.4 ± 0.8 Ma³¹, which overlaps with the range of single-spot ages obtained in this study (0.7–21.6 Ma). However, considering the centimeter-scale age heterogeneity of CT3 revealed in our study, comparisons with age data derived from bulk samples are inherently limited. The dominant age population of sylvite P3 at ~33 Ma is close to the published $^{40}\text{Ar}/^{39}\text{Ar}$ ages of polyhalite (~28–29 Ma)^{19,20,31} It has been suggested that the formation or recrystallization of the latter is linked to tectonic processes associated with the subsidence of the North German Basin.³¹ Contemporaneous fluid activity during this tectonic phase is documented by U-Pb ages of stylolitic magnesite formed by incongruent dissolution-reprecipitation of anhydrite within the Gorleben salt dome (25.5 ± 7.4 Ma, 26.4 ± 3.3 Ma, and 13.4 ± 2.9 Ma).³³

The dominant age mode of P10 sylvite at ~91 Ma closely coincides with the Rb-Sr ID TIMS ages of carnallite from the Salzdettfurth mine located only ~100 km from Morsleben (86 ± 1 and 100 ± 1 Ma).²⁸ These ages may be linked to the onset of late Cretaceous intraplate contraction in central Europe, which is a result of a fundamental change in the relative plate motion between Africa and Europe at ca. 90 Ma.⁷⁶ This tectonic reorganization is characterized by widespread basement thrusting and foreland deformation and likely promoted enhanced fluid circulation and mineral reactions within the salt system, providing favorable conditions for sylvite/carnallite formation and/or isotopic resetting at that time.

3. Conclusion

We have demonstrate that in situ Rb-Sr geochronology of potassium-bearing evaporite minerals is feasible with sufficient precision using 157 nm laser ablation coupled to ICP-MS/MS. Compared to 193 nm radiation, the 157 nm wavelength provides significantly more stable and controlled ablation of sylvite and carnallite, enabling reliable determination of highly radiogenic Rb-Sr isotope ratios despite extremely low common Sr concentrations. The resulting single-spot ages reveal spatially heterogeneous age populations that may record multiple episodes of recrystallization and fluid-mediated isotopic resetting within the Morsleben salt system during the Cretaceous and Cenozoic. These results highlight the potential of high-spatial-resolution Rb-Sr dating of K-salt minerals to directly constrain the tectonic and fluid-flow history of evaporite deposits. By providing insights into the timing and extent of past fluid migration and deformation, such evaporite systems serve as natural experiments over geological timescales. Consequently, they improve predictions of the long-term geochemical stability of salt formations and provide valuable constraints for geological site assessments, particularly in the context of radioactive waste disposal, where safety must be demonstrated over timescales of up to hundreds of thousands of years. In Germany for example the considered assessment period is 1,000,000 year for high-level, heat-generating waste.

5. Data availability and supplementary material

The data present in this article and further supplementary data are available through the Zenodo repository (<https://doi.org/10.5281/zenodo.18399342>).

6. Acknowledgments

1
2
3
4
5
6
7
8
9
10
11
12
13
14
15
16
17
18
19
20
21
22
23
24
25
26
27
28
29
30
31
32
33
34
35
36
37
38
39
40
41
42
43
44
45
46
47
48
49
50
51
52
53
54
55
56
57
58
59
60

Open Access Article. Published on 24 April 2026. Downloaded on 4/24/2026 11:47:55 PM.
This article is licensed under a Creative Commons Attribution 3.0 Unported Licence.



This work is funded by a DFG grant (project ID 5387656229) awarded to MK. LA-ICP-MS/MS equipment funding was provided by DFG Large Equipment Grant INST 161/1073-1 FUGG (to WM). FIERCE is financially supported by the Deutsche Forschungsgemeinschaft (DFG: INST 161/921-1 FUGG, INST 161/923-1 FUGG) and received financial support from the Wilhelm and Else Heraeus Foundation, which is gratefully acknowledged.

We sincerely thank Hartmut Blanke and Mario Patzschke (BGE) for their guidance during our visit to Morsleben in March 2025. Alexander Schmidt (GU) is acknowledged for technical support during LA-ICP-MS/MS analyses. The comments of two journal reviewers helped to improve the clarity of our presentation and are gratefully acknowledged, as is the swift editorial handling throughout.

7. References

- (1) Winterle, J., Ofoegbu, G., Pabalan, R., Manepally, C., Mintz, T., Percy, E., and Fedors, R. Geologic disposal of high-level radioactive waste in salt formations. Contract NRC-02-07-006. US Nuclear Regulatory Commission, (2012).
- (2) von Berlepsch, T., and Haverkamp, B. Salt as a host rock for the geological repository for nuclear waste. *Elements*, 12, (2016), 257-262.
- (3) Williams, J. D. O., Williamson, J. P., Parkes, D., Evans, D. J., Kirk, K. L., Sunny, N., Hough, E., Vosper, E., and Akhurst, M. C. Does the United Kingdom have sufficient geological storage capacity to support a hydrogen economy? Estimating the salt cavern storage potential of bedded halite formations. *Journal of Energy Storage*, 53, (2022), 105109.
- (4) Miocic, J., Heinemann, N., Edlmann, K., Scafidi, J., Molaei, F., and Alcalde, J. Underground hydrogen storage: a review. Geological Society, London, Special Publications, (2023), 73-86.
- (5) Liu, W., Li, Q., Yang, C., Shi, X., Wan, J., Jurado, M. J., Li, Y., Jiang, D., Chen, J., Qiao, W., Zhang, X., Fan, J., Peng, T., and He, Y. The role of underground salt caverns for large-scale energy storage: A review and prospects. *Energy Storage Materials*, 63, (2023), 103045.
- (6) Liu, W., Chen, J., Jiang, D., Shi, X., Li, Y., Daemen, J. J. K., and Yang, C. Tightness and suitability evaluation of abandoned salt caverns served as hydrocarbon energies storage under adverse geological conditions (AGC). *Applied Energy*, 178, (2016), 703-720.
- (7) Raymond, J., Langevin, H., Comeau, F.-A., and Malo, M. Temperature dependence of rock salt thermal conductivity: Implications for geothermal exploration. *Renewable Energy*, 184, (2022), 26-35.

1
2
3
4
5
6
7
8
9
10
11
12
13
14
15
16
17
18
19
20
21
22
23
24
25
26
27
28
29
30
31
32
33
34
35
36
37
38
39
40
41
42
43
44
45
46
47
48
49
50
51
52
53
54
55
56
57
58
59
60

Open Access Article. Published on 24 April 2025. Downloaded on 4/24/2026 11:47:55 PM.
This article is licensed under a Creative Commons Attribution 3.0 Unported Licence.



- 1
2
3
4 (8) Chang, J., Qi, Y., Yang, R., and Hao, T. The self-healing property of rock salt damage in underground gas
5 storage: A review. *Results in Engineering*, 27, (2025), 106098.
- 6
7
8 (9) Orris, G. J., Cocker, M. D., Dunlap, P., Wynn, J. C., Spanski, G. T., Briggs, D. A., and Gass, L. Potash: a
9 global overview of evaporite-related potash resources, including spatial databases of deposits, occurrences, and
10 permissive tracts. U.S. Geological Survey Scientific Investigations Report, 2010-5090-S, (2014).
- 11
12 (10) Dickin, A. P. *Radiogenic Isotope Geology*, 2nd edn, Cambridge University Press, New York, (2005).
- 13
14 (11) Pilot, J., and Blank, P. K-Ar-Bestimmungen von Salzgesteinen des Zechsteins. *Zeitschrift für angewandte
15 Geologie*, 13, (1967), 661-662.
- 16
17 (12) Wardlaw, N. C. Carnallite-Sylvite Relationships in the Middle Devonian Prairie Evaporite Formation,
18 Saskatchewan. *Geological Society of America Bulletin*, 79, (1968), 1273-1294.
- 19
20 (13) Brookins, D. G., Register, J. K., and Krueger, H. W. Potassium-argon dating of polyhalite in southeastern
21 New Mexico. *Geochimica et Cosmochimica Acta*, 44, (1980), 635-637.
- 22
23 (14) Brookins, D. G., Krueger, H. W., and Bills, T. M. Rb-Sr and K-Ar analyses of evaporite minerals from
24 southeastern New Mexico. *Isotopes*, 43, (1985), 11-12.
- 25
26 (15) Lippolt, H. J., Hautmann, S., and Pilot, J. 40Ar/39Ar-Dating of Zechstein Potash salts: New constraints on
27 the numerical age of the Latest Permian and the P-Tr boundary. *Terra Abstracts*, Suppl. No. 1 to *Terra Nova*, 5,
28 (1993), 591.
- 29
30 (16) Halas, S., Wójtowicz, A., and Peryt, T. M. K/Ar dates of some Miocene potash salts from Carpathian
31 Foredeep. *Acta Geol Hun*, 39, (1996), 64-67.
- 32
33 (17) Léost, I., Fraud, G., Blanc-Valleron, M. M., and Rouchy, J. M. First absolute dating of Miocene
34 langbeinite evaporites by 40Ar/39Ar laser step-heating: [K2Mg2(SO4)3] Stebnyk mine (Carpathian Foredeep
35 Basin). *Geophysical Research Letters*, 28, (2001), 4347-4350.
- 36
37 (18) Wójtowicz, A., Hryniv, S. P., Peryt, T. M., Bubniak, A., Bubniak, I., and Bilanizhka, P. M. K/Ar dating of
38 the Miocene potash salts of the Carpathian foredeep (West Ukraine): Application to dating of tectonic events.
39 *Geologica Carpathica*, 54, (2003), 243-249.
- 40
41 (19) Neubauer, F., Leitner, C., Schorn, A., and Genser, J. Dating of sulphates and their deformation structures:
42 preliminary results from German Zechstein and Austrian Haselgebirge. *Fragile Earth*, Munich International
43 Conference Abstracts with Programs, 4, (2011).
- 44
45 (20) Neubauer, F., Schorn, A., Genser, J., and Leitner, C. Ar-Ar dating of polyhalite and langbeinite in
46 evaporite bodies. *Goldschmidt 2014 Abstracts*, (2014), 1789.
- 47
48 (21) Leitner, C., Neubauer, F., Genser, J., and Bernroder, M. Dating of polyhalite: a difficult 40Ar/39Ar dating
49 tool of diagenetic to very low-grade metamorphic processes. *International Journal of Earth Sciences*, 111,
50 (2022), 2037-2051.
- 51
52 (22) Plevaya, N. I., Titov, N. E., Belayev, V. S., and Sprintsson, V. D. Application of the Ca method in the
53 absolute age determination of sylvite. *Geochemistry*, 8, (1958), 897-906.
- 54
55 (23) Wilhelm, H. G., and Ackermann, W. Altersbestimmung nach der K-Ca-Methode an Sylvin des Oberen
56 Zechsteins des Werragebietes. *Zeitschrift für Naturforschung A*, 27, (1972), 1256-1259.
- 57
58
59
60

- (24) Obradovich, J. D., Tatsumoto, M., Manuel, O. K., Mehnert, H., Domenick, M., and Wildman, T. K. Ar and K-Ca dating of Sylvite from the Late Permian Salado Formation, New Mexico. Implications regarding Stability of Evaporite Minerals. Abstracts Fifth International Conference on Geochronology, Cosmochronology, Isotope Geology, Nikko National Park, Japan, 27.6.-2.7.1982, (1982), 283-284.
- (25) Baadsgaard, H. Rb-Sr and K-Ca isotope systematics in minerals from potassium horizons in the Prairie Evaporite Formation, Saskatchewan, Canada. *Chemical Geology*, 66, (1987), 1-15.
- (26) Henjes-Kunst, F., Prochaska, W., and Schramm, M. Application of the Sm-Nd isochron method to dating of evaporitic and hydrothermal carbonates. *Goldschmidt Conference Abstracts 2008*, (2008), A368.
- (27) Oesterle, F.-P., and Lippolt, H. J. Isotopische Datierung der Langbeinitbildung in der Kalisalzlagerstätte des Fulda Beckens. *Kali und Steinsalz*, 6, (1975), 391-398.
- (28) Lippolt, H. J., and Raczek, I. Cretaceous Rb-Sr Total Rock Ages of Permian Salt Rocks. *Naturwissenschaften*, 66, (1979), 422-423.
- (29) Philippe, S., and Haack, U. Rb-Sr study on langbeinite and other salt minerals from a Zechstein diapir in northern Germany. *Chemical Geology*, 123, (1995), 199-207.
- (30) Philippe, S., and Haack, U. Rb-Sr Systematics in Carnallitites and Carnallitic Rocks from the German Zechstein. *Geologisches Jahrbuch, Reihe E*, 57, (1997), 3-21.
- (31) Mertineit, M., Hammer, J., and Schramm, M. Alterbestimmung von Kluftmineralisationen und Deformationsprozessen in Salinargesteinen. *Zwischenbericht 9Y3203000000*, BGR, Hannover, (2015).
- (32) Beranoaguirre, A., Vasiliev, I., and Gerdes, A. In situ LA-ICPMS U-Pb dating of sulfates: applicability of carbonate reference materials as matrix-matched standards. *Geochronology*, 4, (2022), 601-616.
- (33) Zulauf, G., Axel, G., Hezel, D., Hohlmeier, B., Linckens, J., and Mertineit, M. Tectonic stylolites in anhydrite rock: Constraints on fluid-assisted deformation and isotopic ages of salt rocks (Gorleben salt dome, Germany). *SSRN*, (2025), <https://dx.doi.org/10.2139/ssrn.5929693>.
- (34) Yi, J., Kirkland, C. L., Bourdet, J., Barham, M., Danišik, M., Feitz, A., Haines, P. W., McDonald, B., Ribeiro, B. V., Frery, E., and Delle Piane, C. Taken with a grain of salt: Resolving evaporite stratigraphy through accessory mineral geochronology. *Earth and Planetary Science Letters*, 671, (2025), 119616.
- (35) Yi, J., Kirkland, C. L., Barham, M., Danišik, M., and Feitz, A. Accessory mineral dating of the Boree Salt in the Adavale Basin, Queensland, Australia. *Journal of the Geological Society*, 183, (2025), jgs2025-171.
- (36) Shannon, R. D. Revised ionic radii and systematic studies of interatomic distances in halides and chalcogenides. *Acta Crystallographica Part A*, 32, (1976), 751-767.
- (37) Harrison, T. M., Célrier, J., Aikman, A. B., Hermann, J., and Heizler, M. T. Diffusion of ^{40}Ar in muscovite. *Geochimica et Cosmochimica Acta*, 73, (2009), 1039-1051.
- (38) Scharf, A., Handy, M. R., Schmid, S. M., Favaro, S., Masafumi, S., Schuster, R., and Hammerschmidt, K. Grain-size effects on the closure temperature of white mica in a crustal-scale extensional shear zone - implications of in situ $^{40}\text{Ar}/^{39}\text{Ar}$ laser-ablation of white mica for dating shearing and cooling (Tauern Window, Easter Alps). *Tectonophysics*, 674, (2016), 210-226.

- (39) Purdy, J. W., and Jäger, E. K-Ar ages on rock-forming minerals from the central Alps. *Memorie dell'Istituto Geologico della R. Università di Padova*, 30, (1976), 1-31.
- (40) Cliff, R. Isotopic dating in metamorphic belts. *Journal of the Geological Society*, 142, (1985), 97-110.
- (41) Cliff, R. A. Rb-Sr dating of white mica - new potential in metamorphic geochronology. *Abstracts ICOG 8*, U.S. Geological Survey Circular 1107, (1994), 62.
- (42) Steck, A., and Hunziker, J. C. The Tertiary structural and thermal evolution of the Central Alps - compressional and extensional structures in an orogenic belt. *Tectonophysics*, 238, (1994), 229-254.
- (43) Villa, I. M. Isotopic closure. *Terra Nova*, 10, (1998), 42-47.
- (44) Glodny, J., Kühn, A., and Austrheim, H. Diffusion versus recrystallization processes in Rb-Sr geochronology: Isotopic relics in eclogite facies rocks, Western Gneiss Region, Norway. *Geochimica et Cosmochimica Acta*, 72, (2008), 506-525.
- (45) Gentner, W., Präg, R., and Smits, F. Argonbestimmungen an Kalium-Mineralien II. Das Alter eines Kalilagers im Unteren Oligozän. *Geochimica et Cosmochimica Acta*, 4, (1953), 11-20.
- (46) Gentner, W., Goebel, K., and Präg, R. Argonbestimmungen an Kalium-Mineralien III. Vergleichende Messungen nach der Kalium-Argon- und Uran-Helium-Methode. *Geochimica et Cosmochimica Acta*, 5, (1954), 124-133.
- (47) Müller, W., Mancktelow, N. S., and Meier, M. Rb-Sr microchrons of synkinematic mica in mylonites: an example from the DAV fault of the Eastern Alps. *Earth and Planetary Science Letters*, 180, (2000), 385-397.
- (48) Egli, D., Müller, W., and Mancktelow, N. Laser-cut Rb-Sr microsampling dating of deformational events in the Mont Blanc-Aiguilles Rouges region (European Alps). *Terra Nova*, 28, (2016), 35-42.
- (49) Li, C., Chu, Z., Wang, X., Guo, J., and Wilde, S. A. Determination of $^{87}\text{Rb}/^{86}\text{Sr}$ and $^{87}\text{Sr}/^{86}\text{Sr}$ ratios and Rb-Sr contents on the same filament loading for geological samples by isotope dilution thermal ionization mass spectrometry. *Talanta*, 233, (2021), 122537.
- (50) Chu, Z., Cui, T., Meisel, T. C., Li, Y., Li, C., Xu, L., Yang, Y., and Peng, P. OU-9: A potential reference material with high $^{87}\text{Rb}/^{86}\text{Sr}$ and $^{87}\text{Sr}/^{86}\text{Sr}$ for data quality control and method validation in ID-MS Rb-Sr Geochronology. *Geostandards and Geoanalytical Research*, (2025), 425-437.
- (51) Zack, T., and Hogmalm, K. J. Laser ablation Rb/Sr dating by online separation of Rb and Sr in an oxygen-filled reaction cell. *Chemical Geology*, 437, (2016), 120-133.
- (52) Hogmalm, K. J., Zack, T., Karlsson, A. K.-O., Sjöqvist, A. S. L., and Garbe-Schönberg, D. In situ Rb-Sr and K-Ca dating by LA-ICP-MS/MS: an evaluation of N_2O and SF_6 as reaction gases. *Journal of Analytical Atomic Spectrometry*, 32, (2017), 305-313.
- (53) Bolea-Fernandez, E., Van Malderen, S. J. M., Balcaen, L., Resano, M., and Vanhaecke, F. Laser ablation-tandem ICP-mass spectrometry (LA-ICP-MS/MS) for direct Sr isotopic analysis of solid samples with high Rb/Sr ratios. *Journal of Analytical Atomic Spectrometry*, 31, (2016), 464-472.
- (54) Moens, L. J., Vanhaecke, F., Bandura, D. R., Baranov, V. I., and Tanner, S. D. Elimination of isobaric interferences in ICP-MS using ion-molecule reaction chemistry: Rb/Sr age determination of magmatic rocks, a case study. *Journal of Analytical Atomic Spectrometry*, 16, (2001), 991-994.

1
2
3
4
5
6
7
8
9
10
11
12
13
14
15
16
17
18
19
20
21
22
23
24
25
26
27
28
29
30
31
32
33
34
35
36
37
38
39
40
41
42
43
44
45
46
47
48
49
50
51
52
53
54
55
56
57
58
59
60


Open Access Article. Published on 24 April 2025. Downloaded on 4/24/2026 11:47:55 PM.
This article is licensed under a Creative Commons Attribution 3.0 Unported Licence.



- (55) Bandura, D. R., Baranov, V., Litherland, A., and Tanner, S. D. Gas-phase ion-molecule reactions for resolution of atomic isobars: AMS and ICP-MS perspectives. *International Journal of Mass Spectrometry*, 255-256, (2006), 312-327.
- (56) Erhardt, T., Norris, A., Rittberger, R., Shelley, M., Kutzschbach, M., Marko, L., Schmidt, A., and Müller, W. Rationale, design and initial performance of a dual-wavelength (157 & 193 nm) cryo-LA-ICP-MS/MS system. *Journal of Analytical Atomic Spectrometry*, 40, (2025), 2857-2869.
- (57) Russo, R. E., Mao, X. L., Borisov, O. V., and Liu, H. Influence of wavelength on fractionation in laser ablation ICP-MS. *Journal of Analytical Atomic Spectrometry*, 15, (2000), 1115-1120.
- (58) Telouk, P., Rose-Koga, E., and Albarède, F. Preliminary results from a new 157 nm laser ablation ICP-MS instrument: New opportunities in the analysis of solid samples. *Geostandards Newsletter*, 27, (2003), 5-11.
- (59) Behlau, J., and Mingerzahn, G. Geological and tectonic investigations in the former Morsleben salt mine (Germany) as a basis for the safety assessment of a radioactive waste repository. *Engineering Geology*, 61, (2001), 83-97.
- (60) Best, G., and Zirngast, M. Die strukturelle Entwicklung der exhumierten Salzstruktur 'Oberes Allertal'. Bundesanstalt für Geowissenschaften und Rohstoffe, Hannover, (2002), 114 pp.
- (61) Brandes, C., Schmidt, C., Tanner, D. C., and Winsemann, J. Paleostress pattern and salt tectonics within a developing foreland basin (north-western Subherzynian Basin, northern Germany). *International Journal of Earth Sciences*, 102, (2013), 2239-2254.
- (62) Behlau, J., Mingerzahn, G., and Bornemann, O. Erarbeitung eines geologischen Lagerstättenmodells Morsleben. Final Report. Bundesanstalt für Geowissenschaften und Rohstoffe, Hannover, (1997), 73 pp.
- (63) Nikonow, W., and Rammlmair, D. Risk and benefit of diffraction in Energy Dispersive X-Ray fluorescence mapping. *Spectrochimica Acta Part B: Atomic Spectroscopy*, 125, (2016), 120-126.
- (64) Kutzschbach, M., Glodny, J., Erhardt, T., and Müller, W. Rb-Sr age resetting by diffusion and neo-/recrystallization in amphibolite-facies metamorphic white mica revealed by micrometer scale LA-ICP-MS/MS mapping. *Chemical Geology*, 712, (2026), 123393.
- (65) Müller, W., Shelley, M., Miller, P., and Broude, S. Initial performance metrics of a new custom-designed ArF excimer LA-ICPMS system coupled to a two-volume laser-ablation cell. *Journal of Analytical Atomic Spectrometry*, 24, (2009), 209-214.
- (66) Woodhead, J. D., and Hergt, J. M. Strontium, neodymium and lead isotope analyses of NIST glass certified reference materials: SRM 610, 612, 614. *Geostandards Newsletter*, 25, (2001), 261-266.
- (67) Wise, S. A., and Watters, R. L. Certificate of Analysis: Standard Reference Material 610. National Institute of Standards and Technology, Gaithersburg, USA, (2012).
- (68) Wise, S. A., and Watters, R. L. Certificate of Analysis: Standard Reference Material 612. National Institute of Standards and Technology, Gaithersburg, USA, (2012).
- (69) Jochum, K. P., Willbold, M., Raczek, I., Stoll, B., and Herwig, K. Chemical characterization of the USGS reference glasses GSA-1G, GSC-1G, GSD-1G, GSE-1G, BCR-2G, BHVO-2G and BIR-1G using EPMA, ID-TIMS, ID-ICP-MS and LA-ICP-MS. *Geostandards and Geoanalytical Research*, 29, (2005), 285-302.

1
2
3
4
5
6
7
8
9
10
11
12
13
14
15
16
17
18
19
20
21
22
23
24
25
26
27
28
29
30
31
32
33
34
35
36
37
38
39
40
41
42
43
44
45
46
47
48
49
50
51
52
53
54
55
56
57
58
59
60

Open Access Article. Published on 24 April 2025. Downloaded on 4/24/2026 11:47:55 PM.
This article is licensed under a Creative Commons Attribution 3.0 Unported Licence.



- (70) Schramm, M., and Mertineit, M. Stoffliche und mikrostrukturelle Untersuchungen zur Entstehung von Salzgesteinen in flacher Lagerung und in Salzstöcken. BGR Hannover, F+E Endlagerung, Abschlussbericht 9Y321502000, (2022).
- (71) Kutzschbach, M., and Glodny, J. LA-ICP-MS/MS-based Rb-Sr isotope mapping for geochronology. *Journal of Analytical Atomic Spectrometry*, 39, (2024), 455-477.
- (72) Norris, A., and Danyushevsky, L. Towards Estimating the Complete Uncertainty Budget of Quantified Results Measured by LA-ICP-MS. Goldschmidt, Boston, 2018-08-12, (2018).
- (73) Villa, I., De Bièvre, P., Holden, N., and Renne, P. IUPAC-IUGS recommendation on the half life of ⁸⁷Rb. *Geochimica et Cosmochimica Acta*, 164, (2015), 382-385.
- (74) Vermeesch, P. IsoplotR: a free and open toolbox for geochronology. *Geoscience Frontiers*, 9, (2018), 1479-1493.
- (75) Marks, M. A. W., Kendrick, M. A., Eby, G. N., Zack, T., and Wenzel, T. The F, Cl, Br, and I contents of reference glasses BHVO-2G, BIR-1G, BCR-2G, GSD-1G, GSE-1G, NIST SRM 610 and NIST SRM 612. *Geostandards and Geoanalytical Research*, 41, (2017), 107-122.
- (76) Longerich, H. P., Jackson, S. E., and Günther, D. Inter-laboratory note. Laser ablation inductively coupled plasma mass spectrometric transient signal data acquisition and analyte concentration. *Journal of Analytical Atomic Spectrometry*, 11, (1996), 899-904.
- (77) Frenzel, M. Making sense of mineral trace-element data – How to avoid pitfalls in statistical analysis and interpretation. *Ore Geology Reviews*, 159, (2023), 105566.
- (78) Kramm, U., and Wedepohl, K. H. The isotopic composition of strontium and sulfur in seawater of Late Permian (Zechstein) age. *Chemical Geology*, 90, (1991), 253-262.
- (79) Rösel, D., and Zack, T. LA-ICP-MS/MS Single-Spot Rb-Sr Dating. *Geostandards and Geoanalytical Research*, 46, (2022), 143-168.
- (80) Redaa, A., Farkaš, J., Gilbert, S., Collins, A. S., Wade, B., Löhr, S., Zack, T., and Garbe-Schönberg, D. Assessment of elemental fractionation and matrix effects during in situ Rb-Sr dating of phlogopite by LA-ICP-MS/MS: implications for the accuracy and precision of mineral ages. *Journal of Analytical Atomic Spectrometry*, 36, (2020), 322-344.
- (81) Redaa, A., Farkaš, J., Gilbert, S., Collins, A. S., Löhr, S., Casegh, D., Forster, M., Blades, M., and Zack, T. Testing Nano-Powder and Fused-Glass Mineral Reference Materials for In Situ Dating of Glauconite, Phlogopite, Biotite and Feldspar via LA-ICP-MS/MS. *Geostandards and Geoanalytical Research*, 47, (2023), 23-48.
- (82) Glorie, S., Gilbert, S. E., Hand, M., and Lloyd, C. Calibration methods for laser ablation Rb-Sr geochronology: comparisons and recommendation based on NIST glass and natural reference material. *Geochronology*, 6, (2024), 21-36.
- (83) Martha, S. O., Xypolias, P., Cheng, C., Dörr, W., Gerdes, A., Hezel, D. C., Kutzschbach, M., Millonig, L., Schmeling, H., Marschall, H. R., Müller, W., and Zulauf, G. Fast arc retreat in the eastern Mediterranean: constraints from late Campanian forearc deposits (Donusa, Greece). *International Journal of Earth Sciences*, 114, (2025), 627-648.
- (84) Dezés, P., Schmid, S. M., and Ziegler, P. A. Evolution of the European Cenozoic Rift System: interaction of the Alpine and Pyrenean orogens with their foreland lithosphere. *Tectonophysics*, 389, (2004), 1-33.

(85) Kley, J., and Voigt, T. Late Cretaceous intraplate thrusting in central Europe: Effect of Africa-Iberia-Europe convergence, not Alpine collision. *Geology*, 36, (2008), 839-842.

Tables

Table 1 Mean trace element concentration and percentage of radiogenic ^{87}Sr of the investigated K-salts, obtained using LA-ICP-MS/MS and μ -XRF.

Element	CT3		P3		P10	
	ROI1	ROI2	mean	2 SE (abs)	mean	2 SE (abs)

1
2
3
4
5
6
7
8
9
10
11
12
13
14
15
16
17
18
19
20
21
22
23
24
25
26
27
28
29
30
31
32
33
34
35
36
37
38
39
40
41
42
43
44
45
46
47
48
49
50
51
52
53
54
55
56
57
58
59
60

Open Access Article. Published on 24 April 2020. Downloaded on 4/24/2026 11:47:35 PM.
This article is licensed under a Creative Commons Attribution 3.0 Unported Licence.



	mean	2 SE (abs)	mean	2 SE (abs)				
Li	0.012	0.0055	<DL		0.015	0.002	0.048	0.015
B	0.64	0.027	0.29	0.032	0.79	0.13	0.39	0.089
Na	<DL		<DL		8700	830	14000	2500
Mg	92000	350	91000	1100	1.4	2	8.4	12
Al	0.19	0.32	0.041	0.0031	0.049	0.0036	0.06	0.023
Si	51	1.6	49	1.4	85	1.3	100	1.6
S	65	2.7	62	3.9	68	1.9	84	11
Ca	<DL		<DL		<DL		<DL	
Rb	330	4.6	340	2.9	46	0.69	110	1.3
Rb (μ XRF)	356	1.5	346	2	43	0.5	65	2.5
Br (μ XRF)	2718	4	2629	5.4	1067	2.6	3074	17.1
^{86}Sr	0.00011	0.00014	0.000051	0.000033	0.000034	0.0000079	0.00048	0.00013
^{87}Sr	0.017	0.0011	0.0054	0.0019	0.006	0.00045	0.039	0.00096
^{88}Sr	0.00075	0.0011	0.00019	0.000087	0.00011	0.000028	0.0036	0.00091
Cs	11.6	0.18	12.1	0.13	0.0079	0.0006	0.014	0.00089
Ba	0.31	0.16	0.13	0.076	0.27	0.033	0.35	0.1
Pb	0.0024	0.0025	0.0018	0.00063	1	0.37	0.013	0.018
U	0.12	0.00021	0.12	0.085	0.13	0.093	0.13	0.002
$^{87}\text{Sr}^*$ (%) ^a	99.5		98.5		99.6		99.1	

all values are expressed as $\mu\text{g/g}$.

DL = detection limits calculated following the approach of Longerich et al. (1996)

For assignment of ROI1/ROI2 compare Fig. 1

Complete table containing the individual analyses is provided in the Table S1

^a amount of radiogenic ^{87}Sr calculated assuming an initial (non-radiogenic) $^{87}\text{Sr}/^{86}\text{Sr}$ ratio of 0.72

Figure captions

Figure 1. Reflected-light images and μ -XRF element maps of the investigated K-salt samples. Sample CT3 consists of pure carnallite ($\text{KMgCl}_3 \cdot 6\text{H}_2\text{O}$), whereas sample P3 is composed of pure sylvite (KCl). Sample P10 represents an intergrowth of sylvite, halite (NaCl), and kieserite ($\text{MgSO}_4 \cdot \text{H}_2\text{O}$). Carnallite is depicted in cyan, reflecting its composition as a mixed potassium-magnesium chloride; the color results from the combination of yellow (K) and blue (Mg). White spots mark the locations of the LA-ICP-MS/MS analyses. Selected spots are labelled with the corresponding Rb-Sr ages. The full set of analytical spots is shown in supplementary Figure S1.

Figure 2. Environmental secondary electron images of ablation pits produced after 300 laser pulses at wavelengths of 157 nm (2.5 J/cm^2) and 193 nm (1.5 J/cm^2). (a) and (b) show concentric backscattered electron images of sylvite P3. At 193 nm, pronounced chipping is observed at the crater edges, whereas ablation at 157 nm produces pits characterized by smooth crater walls and bottoms. (c) and (d) show concentric backscattered electron images of carnallite CT3. For CT3, ablation at 193 nm is characterized by markedly higher ablation rates and crater bottoms exhibiting pronounced surface roughness and strong tapering with depth, as further illustrated in the large-field secondary electron image in (e). In contrast, ablation at 157 nm results in smooth, well-defined ablation pits with an approximately cylindrical geometry.

Figure 3 LA-ICP-MS/MS signals acquired during static spot ablation of (a) sylvite P3 (spot #001) and (b) carnallite CT3 (spot #011) using the 157 nm laser (2.5 J cm^{-2} , 10 Hz, 60 s). The interval selected for quantification (dotted vertical lines) excludes the first 3 s in order to avoid contributions from surface contamination, which is indicated by elevated ^{88}Sr concentrations at the



beginning of the signal. After the first few laser pulses, the ^{88}Sr signal intensity remains close to that of the gas blank, whereas ^{87}Sr consistently is significantly above blank levels, suggesting that nearly all Sr present is derived from radiogenic ingrowth. Moreover, the smoothly declining Sr signal argues against Sr being hosted in (fluid) inclusions. Note the progressive accumulation of Br during ablation of carnallite. (c) Downhole fractionation patterns for sylvite and carnallite compared to those of the analyzed reference materials.

Figure 4 Compilation of single spot Rb-Sr ages obtained for the three investigated potassium salts together with the resulting adaptive Kernel density estimates (KDE). The width of the bars denotes the 2s uncertainty. All single spot ages are also compiled in Table S1. The top part of the figure shows available literature data for salt minerals of Morsleben and other German salt mines located in the proximity. The latter have been recalculated using the ^{87}Rb decay constant of Villa et al. (2015); see Table S2.

1
2
3
4
5
6
7
8
9
10
11
12
13
14
15
16
17
18
19
20
21
22
23
24
25
26
27
28
29
30
31
32
33
34
35
36
37
38
39
40
41
42
43
44
45
46
47
48
49
50
51
52
53
54
55
56
57
58
59
60

Data Availability Statement

The data present in this article and further supplementary data are available through the Zenodo repository (<https://doi.org/10.5281/zenodo.18399342>).

Open Access Article. Published on 24 April 2026. Downloaded on 4/24/2026 11:47:35 PM.
This article is licensed under a Creative Commons Attribution 3.0 Unported Licence.

